Shear-Driven Redistribution of Surfactant Affects Enzyme Activity in Well-Mixed Femtoliter Droplets

Yu Liu, [†] *Seung-Yong Jung,* [†] *and C. Patrick Collier**[, †, ‡]

[†]Division of Chemistry and Chemical Engineering, California Institute of Technology,

Pasadena, California 91125

[‡]Center for Nanophase Materials Sciences, Oak Ridge National Laboratory, P.O. Box 2008, MS-6493,

Oak Ridge, Tennessee 37831

*colliercp@ornl.gov, fax 1 (865) 574-1753

Supporting Information

Table of Contents

Mold fabrication ……. S2

Device fabrication…… S3

Inlet and mixing stability tests …… S4

Plug formation stability…… S6

Droplet size distributions and optical calibration procedures……. S8

Determination of Droplet Diameter…… S8

Determination of Total Fluorescence Signal (I_{tot}) from the Droplet…….. S9

Conversion between I_{tot} and fluorescent resorufin concentration…….. S10

Trapped droplet stability……. S11

Bulk kinetics -- Lineweaver Burk plot…… S12

Control experiments for kinetic data from droplets in Figure 2……. S12

Product inhibition of β-Gal by galactose…… S13

Photoreactions involving singlet oxygen…… S14

Photobleaching…… S14

Loss of ions at interface...…… S16

Correlation plots of enzyme activity, plug length and droplet diameter vs. backing pressure S16

Estimation of capillary number based on the geometry of deformed droplet…… S19

Testing role of interface with inclusion of aqueous PEG600 as crowding agent in droplets S20

Comparison of droplet kinetics with traditional assays for detecting nonspecific adsorption S21

Interfacial tension measurements from pendant drops…… S23

Laser scanning confocal microscopy images of microemulsions…… S25

S/V scaling of enzyme densities in droplets…… S27

Epifluorescent images of daughter droplets containing labeled enzymes…… S29

Calculation of p-value using student t-test in Figure 2B of main text……. S30

Raw data for Figure 2B of main text…… S30

References…… S30

Mold fabrication

Triple-layer photolithography was used to fabricate a silicon master for fabricating PDMS devices by micromolding. Patterns containing the round control button for the control valve, the side channel, and the main channel were drawn in separate layers in AutoCAD 2004 and imaged at 20,000 dot-per-inch resolution onto optical transparencies (CAD/Art Services, Inc., Bandon, OR). To make the control button, a piece of isopropyl alcohol (IPA)-cleaned silicon wafer was spin-coated with positive-tone SPR 220-7 photoresist (Shipley Company, L.L.C., Marlborough, MA) at 4000 rpm. After soft-baking at 115° C for 90 seconds, the resist was exposed to UV light under a photomask for 100 seconds at 14.9 mW/cm^2 on a Karl-Suss MA 6 mask aligner (Suss MicroTec AG, Garching, Germany). MIF-319

developer (Rohm & Haas Electronic Materials, Philadelphia, PA) was used to develop the pattern, followed by rinsing with 18 MΩ water. Overnight baking in an oven at 190° C rounded the feature and stabilized the photoresist. A second layer of AZ 50 positive photoresist (AZ Electronic Materials USA Corp., Branchburg, NJ) was spin-coated at 4000 rpm onto the wafer to make the side channel. The soft bake consisted of three steps: 2 minutes at 65° C, 5 min at 115° C and 2 minutes at 65° C. After aligning the side channel pattern with the control button, UV exposure at 14.9 mW/cm^2 for 50 seconds transferred the pattern from the mask to the wafer. A 4:1 (v/v) mixture of water and 2401 developer (Shipley) was used to develop the pattern. Hard baking at 200° C rounded the side channel and stabilized the AZ 50 resist. For the third layer, corresponding to the main channel, SU8 2025 negative-tone photoresist was spin-coated onto the wafer at 2500 rpm and soft-baked at 65° C for 3 minutes and 95° C for 6 minutes. Following careful alignment of the photomask for the main channel and the side channel already on the master, the wafer was exposed to UV illumination for 20 seconds at 14.9 mW/cm^2. Post-exposure baking at 65° C for 1 minute and 95° C for 6 minutes cross-linked the exposed resist; the remaining non cross-linked residue was removed by immersing the wafer for 1 minute in SU8 developer. The master was then hard baked at 150° C for an additional 10 minutes. The mold for the control valve layer was made by single-layer photolithography using 30 μm-thick SU8 2025 resist with the same baking, exposure and development protocol. All the cross-sectional profiles of the patterns were checked with a profilometer (XP2, AmBios Technology, Inc., Santa Cruz, CA).

Device fabrication

Multi-layer soft-lithography was used to make the three-layer PDMS device. The molds for both the flow and control layers were treated in trimethylchlorosilane (Sigma-Aldrich) vapor for 3 minutes to facilitate the separation of cured PDMS from the molds. 40 g PDMS pre-polymer (RTV 615, GE Silicones, Wilton, CT) with 5:1 mass ratio of base to curing agent was thoroughly mixed for 1 minute, defoamed for 3 minutes, and then poured into a petri dish containing the control mold. Dissolved air in the mixture was further removed by vacuum in a desiccator. The PDMS was partially cured in an oven

at 80° C for 45 minutes. For the flow layer, PDMS pre-polymer with 20:1 mass ratio of base and curing agent was mixed similarly and spin-coated onto the flow mold at 2000 rpm. PDMS of the same composition was also used to spin-coat at 8000 rpm an IPA-cleaned # 0 coverglass (Erie Scientific Company, Portsmouth, NH) to form the bottom layer. The flow and bottom layers were cured at 80° C for 40 minutes and 30 minutes, respectively. The control layer was peeled from its mold, drilled at preset punch marks and aligned with the flow layer. These two layers were bonded together at 80° C for 90 minutes before being peeled away from the flow mold as a monolithic block. Inlet/outlet holes were drilled through the control layer to the main and side channels in the flow layer with 22 gauge blunt-edge needles, and the top two layers were bonded to the PDMS-coated cover glass permanently by heating overnight at 80° C.

Inlet and mixing stability tests

It was critical that the relative rates of injection of the two aqueous streams (enzyme and substrate) into the main channel be balanced by tuning the pressure transducers such that there were always 50/50 mixtures in the mother plugs. This would ensure that the relative concentrations of enzyme and substrate were known accurately when comparing the enzymatic reaction rate as a function of droplet size to the bulk value at the same concentration of enzyme and substrate. We found that pressure fluctuations at the three-way intersection of the aqueous and oil channels, due to changes in radii of curvature of the oil-aqueous interfaces of the plugs, resulted in fluctuations in the position of the boundary line separating the two aqueous streams at the intersection, and hence, the relative concentrations of enzyme and substrate incorporated in each plug. These fluctuations could be minimized however with careful adjustments of the three pressure transducers, which have a guaranteed accuracy of 0.25% (0.1% typical). Figure S1 quantifies the stability of the interface between Alexa568-β-Gal solution and non-fluorescent buffer solution at the intersection of the two aqueous channels by plotting the standard deviation of fluorescence intensity at each pixel from a set of 60 images taken at the inlet. If the interface was perfectly stationary, a peak of zero width would appear in Figure S1. The width of peak in

the center indicates that the error in the final resorufin concentration due to the interface fluctuations was less than 10%. Uncertainties in the initial concentrations of enzyme and substrate of 10% would lead to errors in the estimation of enzymatic reaction rates in the Michaelis-Menten formula of at most, 5%.

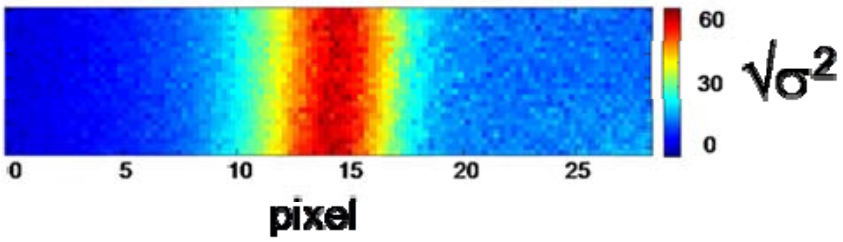

Fig. S1 Standard deviation of intensity at interface between fluorescent and nonfluorescent streams at aqueous inlet of microfluidic device.

As a further test, we injected fluorescently labeled enzymes into one or both of the aqueous inlets and quantified the concentration of labeled enzymes in daughter droplets relative to that in the aqueous inlet(s) for the following three protocols: (1) inject same concentration fluorescent Alexa568-*β*-Gal (13 μg/mL) into both aqueous inlets, (2) mix 1:1 ratio Alexa568-*β*-Gal (13 μg/mL) and reaction buffer first, then inject the mixture into both aqueous inlets, (3) mix 1:1 ratio Alexa568-*β*-Gal (13 μg/mL) and reaction buffer directly on-chip. Table S1 shows that the maximum error in labeled enzyme concentration in the daughter droplets for protocol (3) compared to protocol (2) was about 16 percent, irrespective of droplet diameter, proof that the chip could produce homogeneously-mixed daughter droplets throughout the size range 4 to 10 μm, with reagent compositions identical to mixing in the bulk. Protocol (2) was taken as the standard and its intensity was normalized to be 0.5 since it was supposed to give a 1:1 mixing of enzyme and buffer solutions. Protocol (2) should be compared with (3), which was the on-chip mixture and close to 0.5, within the experimental uncertainty. Solution (1) was enzyme stock only, giving a fluorescent signal about twice that of solution (2).

Table S1. Mixing tests in daughter droplets with fluorescently labeled β-Gal enzymes (concentration of labeled enzymes in daughter droplets relative to that in the aqueous inlets).

Droplet Diameter (μm)	(1) Inject same concentration fluorescent enzymes in both inlets	(2) Inject 50/50 mixture in both inlets	(3) Mix directly on-chip
5.00	0.91±0.06	0.5	0.45±0.06
5.25	0.92±0.06	0.5	0.47±0.08
8.00	0.90±0.04	0.5	0.42±0.09
8.50	0.95±0.03	0.5	0.46±0.04

Plug formation stability

Flow rates of aqueous mother plugs and daughter droplets were determined by analyzing bright field images from the CCD camera at a specific integration time (1-5 msec). The measured length of the blur (in μm) at the leading or trailing edge of a plug or droplet divided by the integration time yielded the linear flow velocity (mm/sec). Averaged results of triplet measurements were recorded. If necessary, flow velocity may be converted to volumetric flow rate (volume/time) using the channel dimensions (see caption to Figure 1 in the manuscript).

The same setup also allowed for photon counting experiments at msec time resolution. These were undertaken to quantify the stability of steady-state plug formation by the device against pressure fluctuations. Fluorescence signal from the steady-state train of plugs containing 0.5 μM resorufin was directed to the side port of the microscope where it was detected by a photon counting module (PCM 942, Perkin-Elmer, Wiesbaden, Germany) and recorded by a digital counter on a NI PCI-6014 multifunction data acquisition board with 2 msec bin times (National Instruments, Austin, TX). A Labview (National Instruments, Austin, TX) program was written to control the data acquisition.

The stability of mother plug formation right before the T-junction was monitored from the fluorescence of resorufin molecules by a photon counting module. Figure S2 shows the histogram of

detected photon numbers. A superposition of a Poisson distribution, corresponding to the background, and a Gaussian distribution, corresponding to the fluorescent signal from plugs, was used to extract the mean and standard deviation of the signal distribution. A threshold, defined as the mean minus three times the standard deviation of the Gaussian distribution, differentiated the raw data points to be either due to background or fluorescence from the plugs.[1]

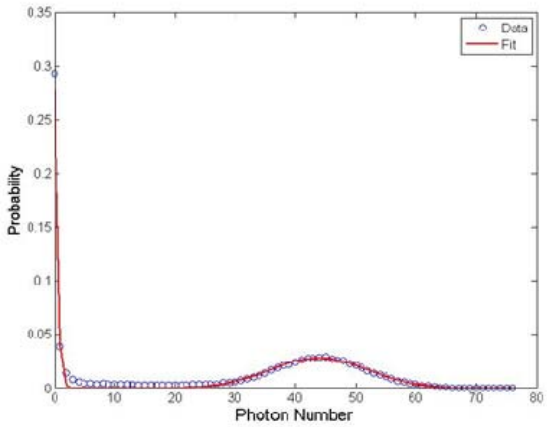

Fig. S2 The histogram of photon number from a train of plugs containing resorufin. The data (circles) are fitted (red) to a linear superposition of a Poisson and a Gaussian distribution with proper normalization.

A typical result is shown in Figure S3. From more than 4000 peaks, we calculated the peak width to be 18±1 ms and the duration between peaks to be 13±1 msec, which corresponds to a plug length of 95 μm and a head-to-tail plug spacing of 69 μm. These values were corroborated by plug length (100 μm) and plug spacing (63 μm) determined from bright field images captured under the same flow conditions with the CCD camera. The standard deviation in peak width was smaller than the time resolution (2 ms) in Figure S3, indicating that plug formation instability due to pressure fluctuations in the system was negligible.

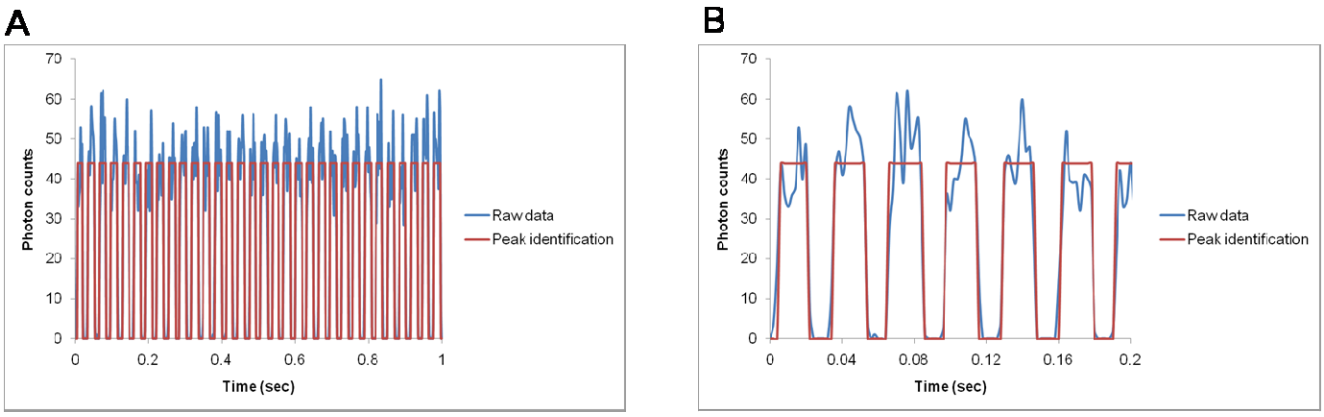

Fig. S3 Time traces of fluorescent plugs moving in the main channel. Raw photon counts (blue) are assigned as signal from plug or background according to a threshold based on the distribution of the raw data. The result from a peak identification algorithm (red) is shown for comparison. More than 4000 peaks in the full trace of 2 minutes could be identified without ambiguity. The first 1 sec (A) and 0.2 sec (B) of the raw data and peak identification are shown.

Droplet size distributions and optical calibration procedures

The optical calibration procedure to determine the concentration of resorufin product as a function of time, and hence, the rate of reaction in different-sized daughter droplets, consisted of three steps: (1) bright field determination of the droplet diameter, (2) determination of the total fluorescence signal from the droplet and (3) determination of the conversion factors relating resorufin concentration to fluorescence signal from different sized droplets.

Determination of Droplet Diameter

Bright-field images of trapped stationary droplets, taken under Köhler illumination conditions, were used to determine droplet diameters according to the following procedure. A bright-field image of an individual droplet was first selected. A rectangular region of interest (ROI) was then drawn about the droplet. Each horizontal line in the ROI was analyzed with a custom made Matlab script to extract the distance between two intensity minima corresponding to a chord length of the droplet. The longest

chord length was taken as the diameter of the droplet. The uncertainty in droplet diameter using this method was about one pixel, or 0.25 μm. Figure S4 shows the relation between droplet diameter distribution and backing pressure at the oil inlet. Size distributions are usually characterized by the coefficient of variation ($COV = std / m$ x 100%, where m and std are the mean and standard deviation of the distribution, respectively). The COV values of the droplet size distributions for our device were less than 3% for all the data sets reported in Figure S4 (seven to nine data points for each set).

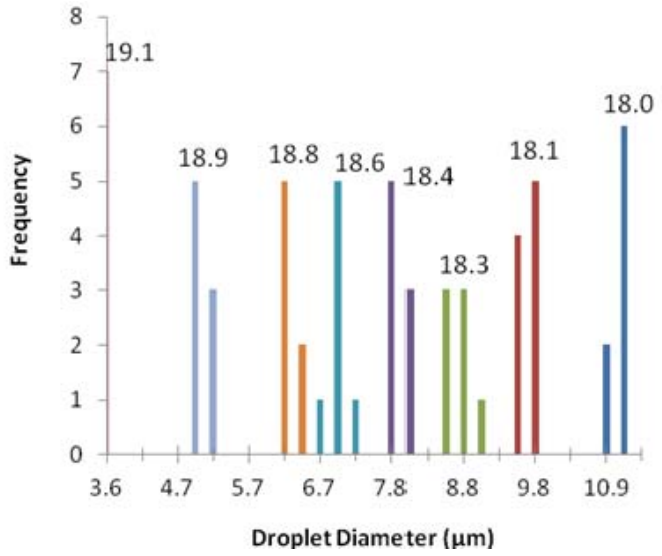

Fig. S4 Daughter droplet size distributions as functions of backing pressure (psi) at the oil inlet. The pressures at the two aqueous inlets were held constant at 16.22 and 16.66 psi. Droplets of desired size can be conveniently generated by tuning oil inlet pressure at fixed aqueous inlet pressures.

Determination of Total Fluorescence Signal (I_{tot}) from the Droplet

The total fluorescence signal (I_{tot}) from the droplet was calculated based on its diameter, which was determined previously from the bright-field image: A rectangular ROI was drawn around a droplet in the fluorescent image. The location of a tentative droplet center was estimated from the image. The tentative droplet center was moved systematically over a user-specified range in order to maximize the integrated fluorescent signal over the area of a circle with the diameter determined in the previous step. The maximum of the integrated signal was used to define the true center of the droplet. Another region

of interest with the same area was then drawn in the vicinity of the droplet to calculate the average background intensity. The maximum of the total signal from the droplet minus the total background signal for the same area defined I_{tot}.

Conversion between I_{tot} and fluorescent product (resorufin) concentration

I_{tot} was a function of both droplet diameter and resorufin concentration. However, since the fluorescence intensity integrated over the circular area of a selected droplet with measured diameter showed a linear relationship with the concentration of resorufin, we were able to determine the resorufin concentration as a function of time in each droplet from a time lapse series of images. This was used to calculate the rate of resorufin concentration increase with time due to enzymatic reactions in droplets. For droplets of the same diameter, I_{tot} was proportional to concentration; hence, the conversion factor for droplets of the same size was given by I_{tot}/c. The concentration in μM was determined from the absorbance of resorufin at 571 nm, using a molar extinction coefficient of 58,000 $M^{-1}cm^{-1}$.[2] Solutions with resorufin concentrations ranging from 0 to 4 μM were prepared by serial dilution from a standard solution at 100 μM, and introduced in both aqueous channels of the microfluidic device to generate fluorescent and bright-field images of droplets of different diameters. In addition to correlating the fluorescent intensity with droplet size, bright-field images of the droplets also ensured that the fluorescent images were focused properly. The average I_{tot} for droplets as a function of size could then be calculated. The absolute concentration of resorufin in the standard solution was determined with a UV/Vis spectrometer (Uvikon 933, Research Instruments International, San Diego, CA). The linear proportionality coefficients used in the calibration of the enzymatic rate data were I_{tot}/c, which varied for different-sized droplets.

Trapped droplet stability

Figure S5 compares bright field images (A, B and C) and fluorescent images (D, E and F) of trapped droplets at different times; no changes in size or position of the droplets were detected after ten minutes. The slight difference between droplets in Figure S5B and C was due to minor drift in the focus of the microscope objective since the boundary of the channel in the two images also appeared to change slightly. Prolonged observation on the same droplet could be performed without ambiguity arising from droplet movement, shrinkage or merging. An alternative process to measure kinetics on a drop by drop basis would be to identify and track a specific moving droplet in real time for sufficiently long times to obtain reliable kinetic information from that droplet. We believe our method is far easier and more amenable for generating large data sets consisting of numerous measurements of different size droplets.

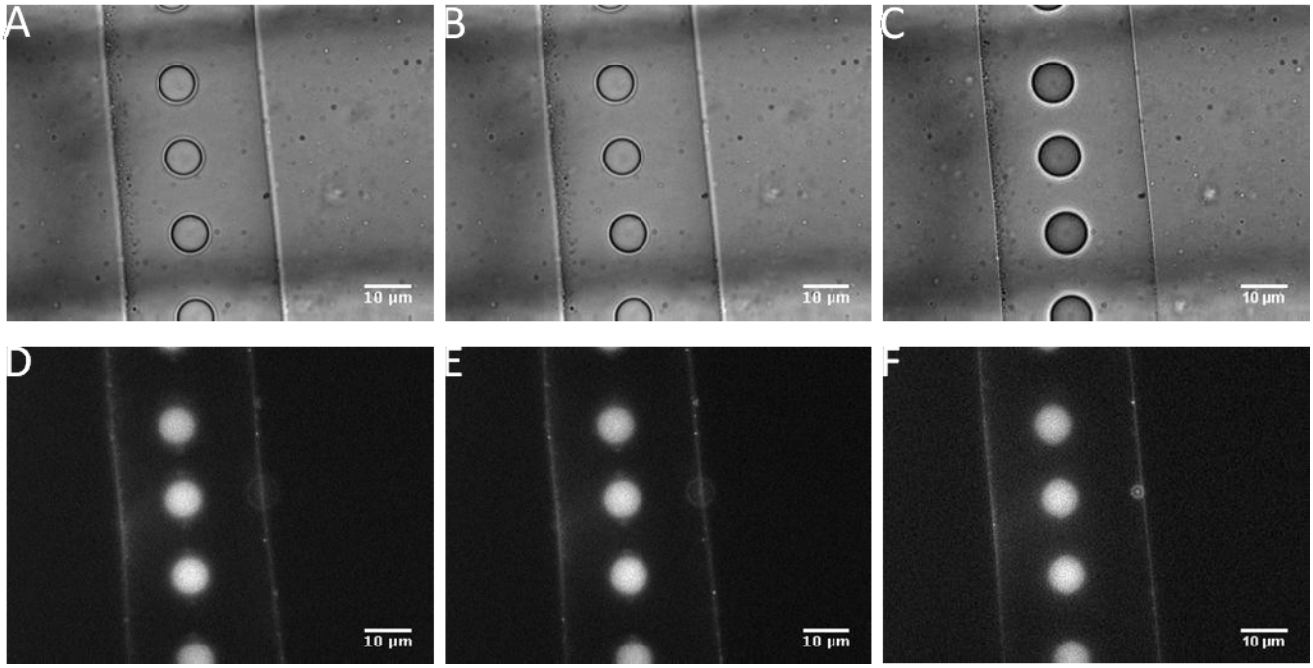

Fig. S5 Droplet stability after being trapped in the side channel by the control valve. Bright field (A, B and C) and fluorescence (D, E and F) images taken when control valve first closed (A, D), three minutes later (B, E) and 10 minutes later (C, F).

Bulk kinetics -- Lineweaver Burk plot

The kinetics of β-Gal/RGP reactions in bulk solution were monitored with a stopped-flow instrument (SX.18MV, Applied Photophysics, Surrey, UK), by measuring the fluorescence increase due to the enzymatic generation of resorufin. Figure S6 is a Lineweaver-Burk (LB) plot[3] from bulk reaction rate data for β-Gal (0.1 μg/mL, 1.85 nM), yielding values of K_M = 128.5 μM and V_{max} = 0.248 μM/sec. The absolute concentration of RGP substrate for each data point in Figure S6 was checked with the UV-Vis spectrometer (ε = 18,000 $M^{-1}cm^{-1}$ at 470 nm).

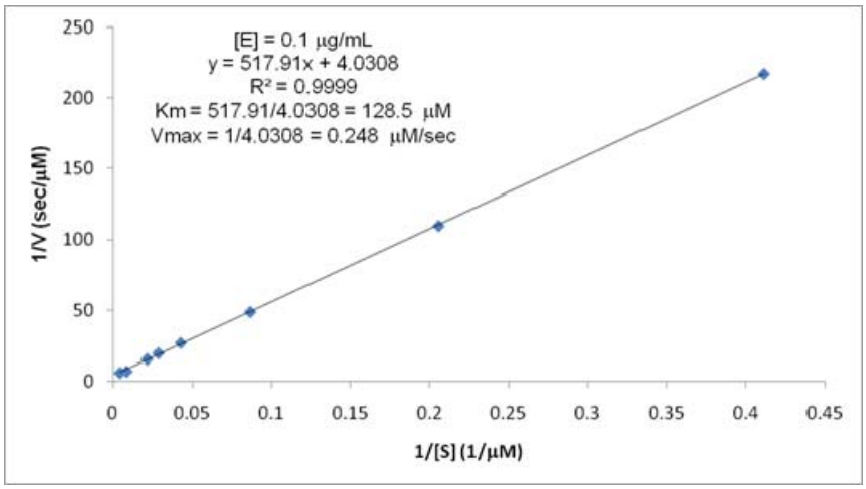

Fig. S6 Lineweaver-Burk plot for β-Gal enzymes, determined from bulk stopped-flow fluorescence measurements

Control experiments for kinetic data from droplets in Figure 2

A number of control experiments were performed to eliminate several other possible causes for the decreased reaction rates in smaller droplets observed in Figure 2 of the manuscript. Consideration of Figure 2A indicates that substrate depletion can be ruled out because the time at which the average bulk rate (0.36 μM/sec) and the fastest droplet rate (from 9.5 μm droplets) diverge, roughly two seconds, corresponds to, at most, the consumption of just 0.7 μM substrate, or roughly three percent of the initial substrate concentration. Bulk absorbance measurements performed both before and after mixing of aqueous solutions containing 50 μM RGP substrate with soy oil containing NP-PEG surfactant did not

show evidence for substrate incorporation in the oil. Inner-filter effects, due to absorption of emitted light from fluorescent resorufin molecules by other product molecules in the droplets, can be ruled out from the calibration curves of fluorescence intensity versus resorufin concentration, which were linear over the concentration range 0 – 4 μM for all droplet sizes.

Product inhibition of β-Gal by galactose

To test whether galactose, a byproduct of the hydrolysis reaction of the RGP substrate by *β*-Gal, can act as a product inhibitor, we carried out a bulk assay of initial enzymatic reaction rates using 10 pM *β*-Gal and 87.5 μM RGP in phosphate buffer, with increasing amounts of added galactose (up to 10 mM). The series of reaction rates was used to generate a dose-response curve and determine the IC_{50} value for galactose inhibition of the reaction.[3] The dose-response plot in Figure S7 suggests an IC_{50} value for 50% galactose inhibition that is well above the maximum concentration of 10 mM used, orders of magnitude beyond what could have been generated by enzymatic hydrolysis of RGP in the microfluidic experiments.

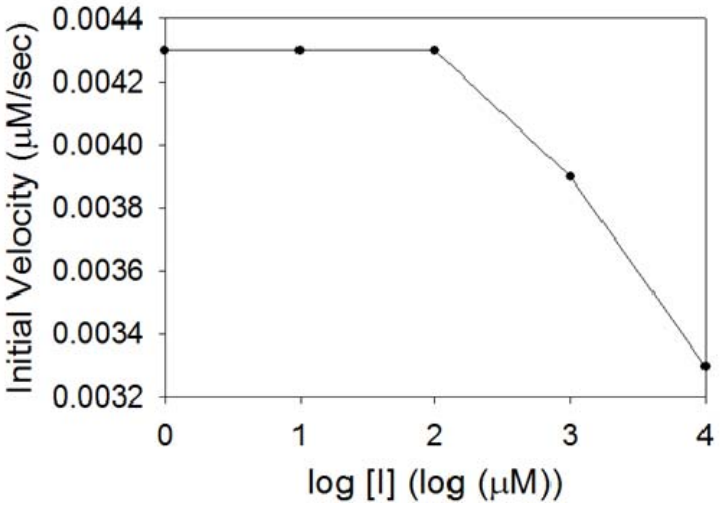

Fig. S7 Dose-response plot of enzyme initial rate as a function of galactose concentration. Enzyme concentration 10 pM and RGP concentration 87.5 μM, in phosphate buffer. From this plot, the IC_{50} value for galactose was greater than 10 mM.

Photoreactions involving singlet oxygen

Figures S8A, B are fluorescence plots of 100 μM RGP substrate alone, and 100 μM substrate with 200 nM resorufin, contained in 5 μm diameter chambers (~100 fL) formed by micromolding in PDMS,[4] under the same illumination conditions as the fL droplet experiments carried out in the microfluidic devices as described in the paper. If there was autohydrolysis of RGP due to reaction with singlet oxygen species generated from the photobleaching of resorufin, we would expect to see significant differences in the relative increases in fluorescence in S8B versus S8A over the time course of five minutes.

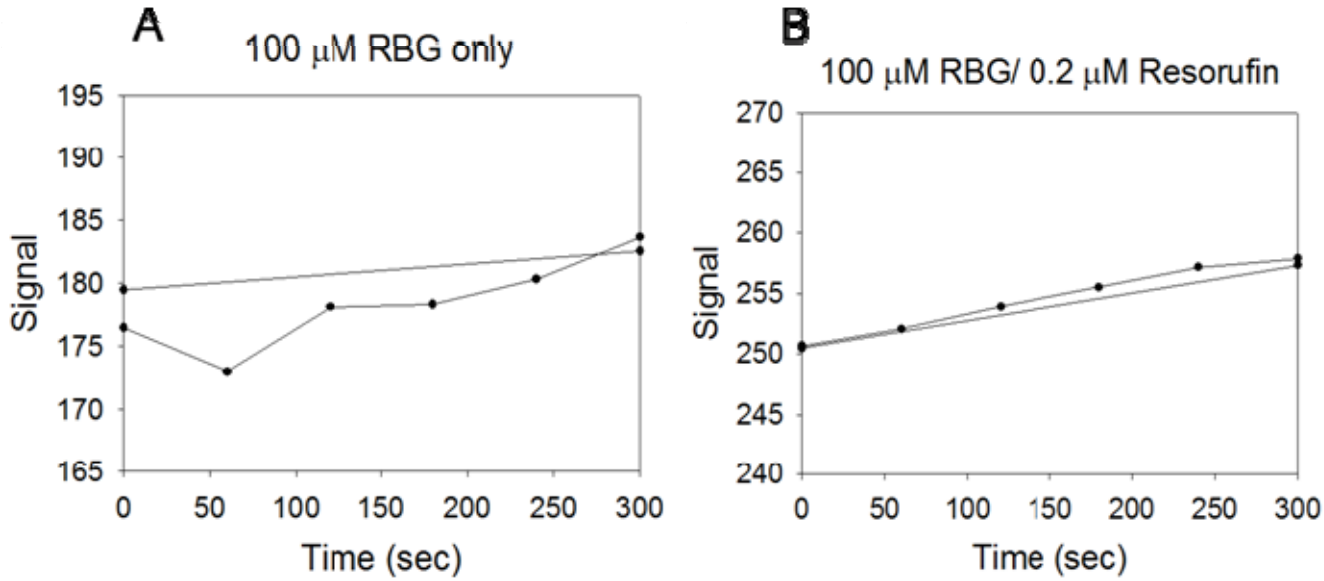

Fig. S8 Fluorescence increases over five minutes measured with CCD camera in 5 μm diameter chambers defined in PDMS containing (A) RGP substrate only, and (B) a mixture of RGP and resorufin. Illumination conditions were the same as for the droplet experiments in the microfluidic devices.

Photobleaching

Figure S9 shows the decrease in resorufin fluorescence due to photobleaching from a 9.5 μm drop (Figure S9A) and from a 6 μm drop (Figure S9B), under the same illumination conditions as used during the experimental determination of enzyme reaction rates. The fitted first-order decay constants

(k_{bleach} = 0.015 s^{-1} for 9.5 μm droplets and 0.029 s^{-1} for 6.0 μm droplets) were then incorporated as an additional decay channel in the Michaelis-Menten formula,

$$\frac{dP(t)}{dt} = \frac{V_{\max} \cdot S(t)}{K_M + S(t)} - k_{bleach} P(t)$$

and then integrated numerically with an ODE solver (MathCAD) using the values for K_M and V_{max} determined from the bulk Lineweaver-Burk plot to simulate the net bulk product concentration as a function of time from competition between product formation due to enzymatic catalysis and loss of fluorescence due to photobleaching. Figure S9C and D show that the effects of photobleaching in the droplets on the bulk kinetic rate are not sufficient to account for the measured decreases in fluorescence, for either size drop.

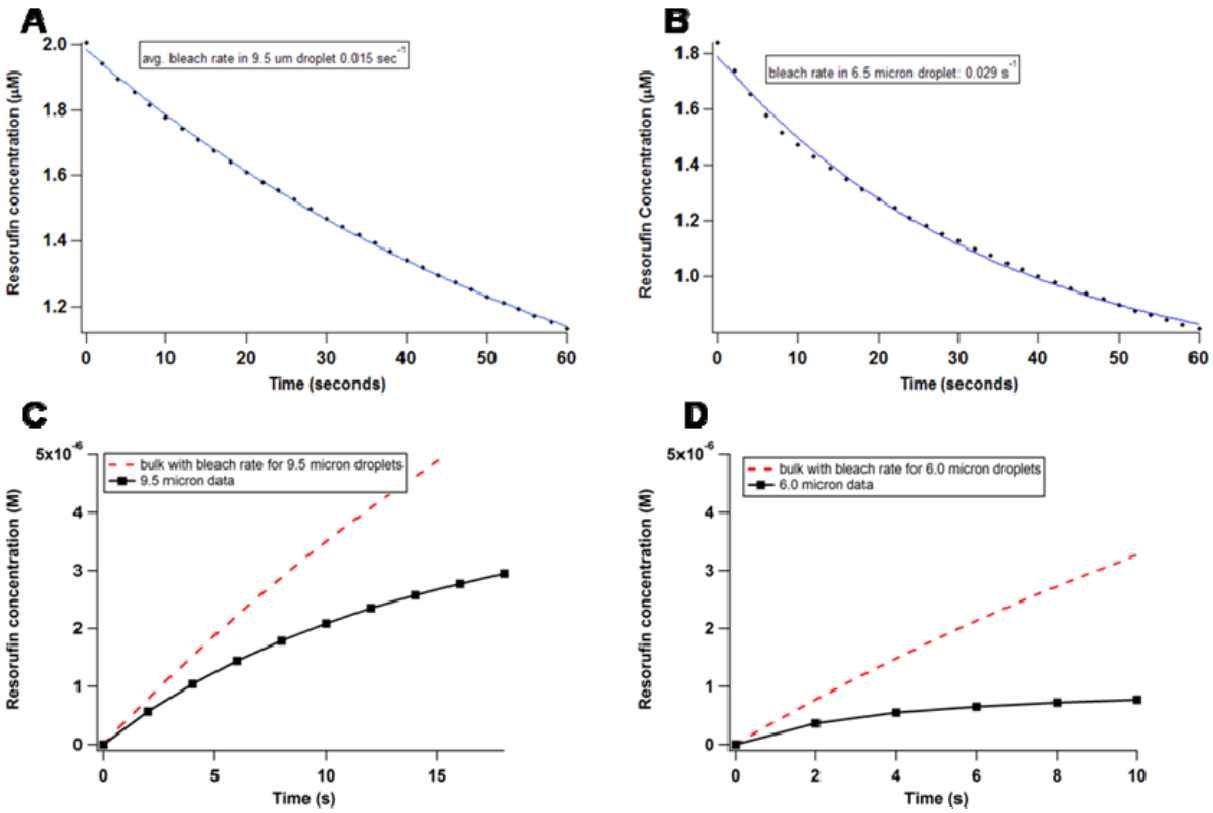

Fig. S9 (A), (B) Plots of fluorescence decay due to photobleaching in daughter droplets 9.5 μm (A) and 6.5 μm (B) in diameter. (C), (D) Plots of simulated enzyme reaction rates when first-order photobleaching decay constants were included in the bulk Michaelis-Menten mechanism, compared to data from the droplets.

Loss of ions at the interface

Additional controls were performed using confocal laser scanning microscopy of water-in-oil microemulsions with droplet sizes in the same range as those generated in the microfluidic devices. Figure S10 shows that inclusion of Magnesium Green dye indicated negligible loss of Mg^{2+} ions in the aqueous droplet interior due to sequestration by PEG groups at the interface,[5] which would negatively affect enzyme activity. Similarly, SNARF-5F 5-(and-6)-carboxylic acid (pKa 7.2) and resorufin (pKa 6.4) dyes indicated the pH did not change in the droplets from their values in the reaction buffer used to prepare the aqueous streams (pH = 7.2) due to loss of hydronium ions at the interface. 1 mg /ml aliquots of these indicators were stored in a minus 20° C freezer or 4° C cold room. Before use, these aliquots were thawed and diluted in reaction buffer (100 mM phosphate buffer with 1mM $MgCl_2$, pH 7.2) to the appropriate concentration. 100µl of purified soybean oil was mixed and stirred with 50 µl of buffer which contained the indicator dyes or fluorescent proteins.

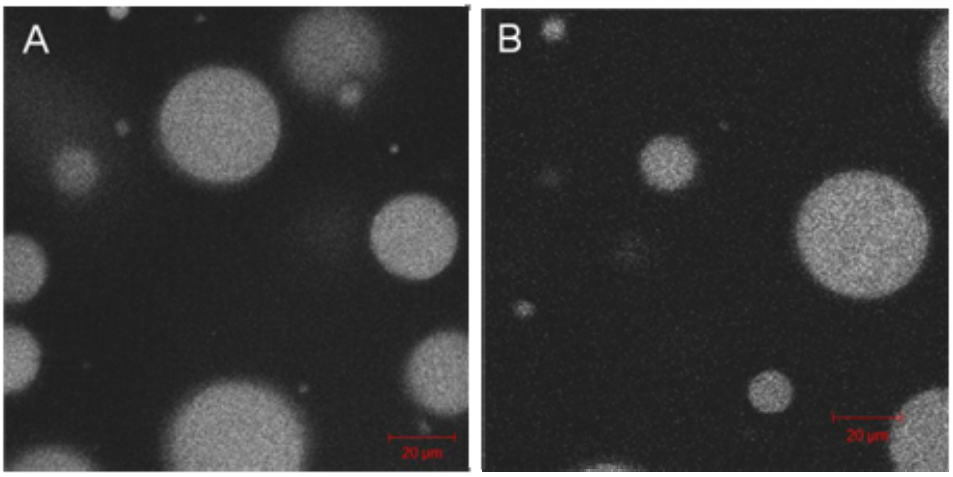

Fig. S10 Fluorescent indicators used to visualize distribution of ions in water-oil microemulsions containing 0.1% v/v NP-PEG. (A) Magnesium Green (B) SNARF.

Correlation plots of enzyme kinetics, plug length and droplet diameter with backing pressure

Figure S11A is a plot of the average fluorescence intensity (background subtracted) versus inverse flow rate in the main channel due to the enzymatic production of resorufin in mother plugs, captured

with the CCD camera just before daughter droplet splitting at the second T-junction. All experimental conditions, including the initial concentrations of enzyme and substrate, and the mixing and initiation of the reaction in the plugs, were the same as those used for the measurements of reaction rates in the daughter droplets described in the manuscript. The data can be grouped into three families classified by the average backing pressures applied at the aqueous inlets (approximately 20 psi, 15 psi and 10 psi). Within each family, mother plugs and daughter droplets of different sizes were intentionally generated by fine-tuning the backing pressure at the oil inlet relative to the fixed backing pressures used at the aqueous inlets. For example, in Figure S11A, the three data points within the "10 psi" ellipse correspond to oil backing pressures of 11.3, 11.5, and 11.6 psi. Tuning the oil backing pressure relative to the fixed aqueous pressures within each family (ellipse) also changed the flow rates of plugs and daughter droplets.

The reciprocal of the flow velocity in Figure S11A multiplied by the distance the plugs travelled from the inlet region to the focal point of the microscope in the main channel (2.3 mm) is simply the reaction time (mixing time) for the β-Gal catalyzed hydrolysis of RGP substrate to give product (roughly 300 to 900 msec, depending on flow velocity). Figures S11B and C are plots of the correlations between flow velocity and average mother plug length in the main channel and average daughter droplet diameter in the side channel, respectively, determined from bright-field images from the CCD camera. Importantly, these plots show that the full range of mother plug lengths (roughly 70 to 90 μm) and daughter droplet diameters (4 to 10 μm) were observed in *each* family (ellipse), which indicates that the size of the plugs and droplets was determined primarily by the minor differences in backing pressures applied at the oil inlet relative to the two aqueous inlets at steady state, and was relatively independent of the magnitude of the average value of the backing pressures. This observation has been reported before for water-in-oil droplets in microfluidic devices.[6]

These correlations in turn indicate that the fluorescence increases in Figure S11A were far more dependent on the reaction time in the plugs before they encountered the second T-junction (which

depended on the flow velocity through the mixer) than on the sizes of plugs (or the resulting daughter droplets after splitting at the junction). While we were not able to convert fluorescence intensity in Figure S11A to absolute resorufin concentrations directly due to the low signal/background from the rapidly moving plugs, the fluorescence increase with transit time should be linearly proportional to the initial enzymatic reaction rate in the plugs, assuming that none of the nominal population of enzymes in the plugs was inactivated. Figure S11A shows that this rate, in fact, was relatively insensitive to changes in plug length, while the reaction rate in the daughter droplets slowed down as a function of their size by as a much as a factor of four compared to the bulk rate, as was shown in Figure 2. We consider this to be strong evidence that the loss of enzyme activity occurred predominately during droplet splitting from the plugs at the second T-junction in the device, and not upstream.

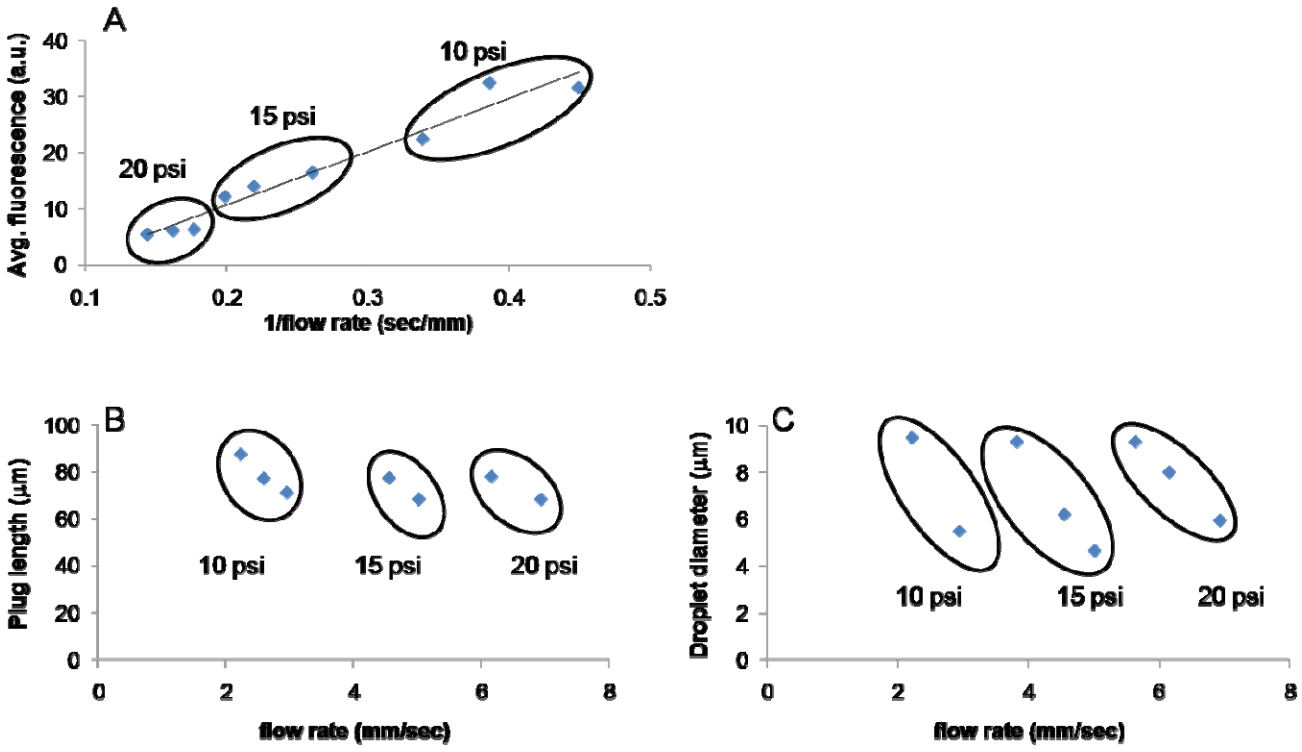

Fig. S11 (A) Average fluorescence intensity versus inverse flow rate from mother plugs in the main channel measured just before splitting of daughter droplets. The data are grouped into three families, classified in the figure by the average backing pressure applied at the aqueous inlets. (B) Plug lengths

and (C) droplet diameters versus flow rate, using the same classification scheme as for (A). The full range of mother plug lengths and daughter droplet diameters were possible in each family of average backing pressure.

Estimation of shear stress based on the geometry of deformed droplet.

Table S1. Determination of shear stresses for nascent daughter droplets at T-junction.

Mean aqueous inlet pressure (psi)	Oil inlet pressure (psi)	Droplet diameter (μm)	Droplet image	$Ca \cong \frac{L-B}{L+B}$	Laplace pressure (kPa)	Shear stress (kPa)
9.9	11.4	9.3	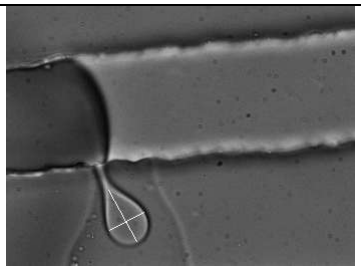	0.21	3.2	0.68
	11.7	5.2	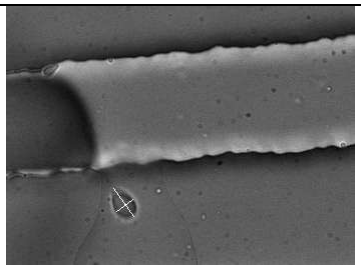	0.27	5.8	1.6
19.7	21.5	8.8	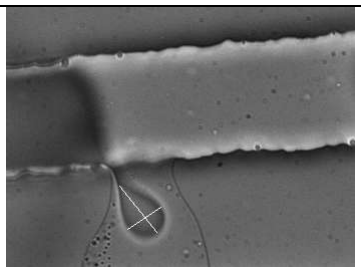	0.20	3.4	0.68
	22.0	5.7	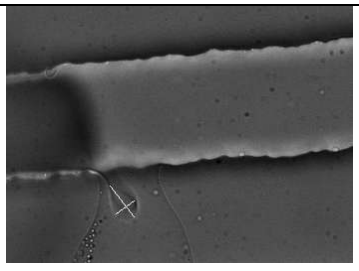	0.30	5.3	1.6

Testing role of interface with inclusion of aqueous PEG600 as crowding agent in droplets

An important prediction of our model is that the size-dependence of the reaction rate decrease in femtoliter droplets would disappear, regardless of the strength of shear stress at the oil-water interface, if the interface could be completely passivated by a high enough concentration of NP-PEG surfactant. However, we could not test this prediction directly by increasing the amount of NP-PEG (or other surface active molecules, such as blocking proteins like BSA) since increased concentrations resulted in premature breakup of mother plugs at the device inlets, as described earlier. Instead, we used high concentrations (up to 100 mg/mL) of soluble PEG600 in the aqueous phase as a crowding agent to help passivate the interface against nonspecific adsorption of β-Gal enzymes. Although PEG600 is not surface active, at the high concentrations used, we expect the interface would be occupied primarily by PEG600 molecules due to excluded volume effects and reduced diffusion coefficients.[7] In addition, PEG600 can form extended hydrogen-bonded networks with the NP-PEG surfactant molecules already present at the interface.[8]

It is well known that molecular crowding affects reaction rates, however, these effects should depend primarily on the concentration of crowders in the aqueous environment, not on the size of the reaction vessel (droplet) itself, and should therefore be the same (within experimental uncertainty) for large and small droplets, as well as the bulk, as long as the concentration of crowders were the same.[9,10] The inclusion of crowding agent thus serves as a test for the importance of the oil-water interface in the size-dependent kinetics we observed (in Figure 2) by limiting the importance of enzyme adsorption at the interface in affecting reaction rates. We first tested the efficiency of the mixing stage of the device for mixing the more viscous solutions containing up to 100 mg/mL PEG-600 using fluorescently-labeled Alexa568-β-Gal enzymes, and found the mixing efficiency to be comparable to that without the crowding agent included in the plugs.

Figure S12 shows that with crowding agent present, the reaction rates in the droplets were comparable to the bulk rate, for all droplet sizes. All other experimental conditions were the same as for the data presented in Figure 2. While not attempting to characterize the mechanisms responsible for lowering enzyme activities with the addition of crowding agents, which have been the subject of many reports in the literature, here we note simply that the addition of the crowding agent has apparently masked the effects that the decrease in passivation at the interface with increasing S/V ratio of the droplets had on enzyme activity. Thus, this experiment serves as an additional control indicating that the decreases in initial enzymatic rates in femtoliter droplets with decreasing diameters seen in Figure 2 (i.e., without crowding agent) were in fact due to progressive inactivation of enzymes resulting from nonspecific adsorption at the oil-water interface.

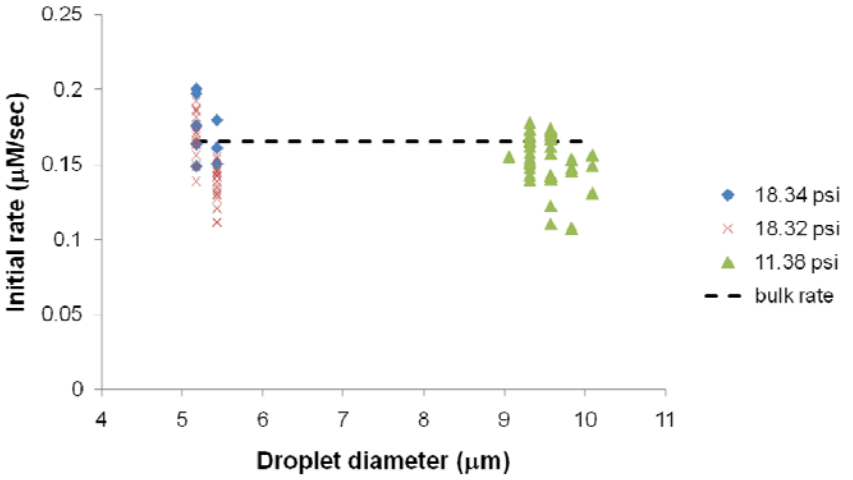

Fig. S12 Initial enzyme reaction rate in large and small daughter droplets, and in the bulk, with inclusion of 100 mg/mL soluble PEG-600 as crowding agent at different backing pressures at the oil inlet.

Comparison of droplet kinetics with traditional assays for detecting nonspecific adsorption

Control of nonspecific interfacial enzyme adsorption in water-oil systems has been demonstrated from interfacial tension measurements with surfactant in the oil phase and proteins in the aqueous phase, and in nanoliter water-in-oil plugs in a microfluidic device by fluorescence microscopy and measurements

of enzyme kinetics.[11] Nonspecific adsorption of β-Gal enzymes without the inclusion of NP-PEG surfactants at the interface was readily apparent from fluorescent images of labeled proteins in emulsion droplets and in mother plugs generated in our microfluidic device, and from interfacial tension measurements using the pendant drop technique. However, there was no evidence for nonspecific adsorption using either fluorescence or tensiometry when 0.1% v/v NP-PEG surfactant was included in the oil, even for enzyme concentrations up to two to three orders of magnitude greater than those used in the droplet experiments on-chip (1.85 nM). Initial reaction rates for β–Gal in larger daughter drops formed in our device (9-10 μm diameter) were close to the average bulk rate. Our observation of minimal change in enzyme activity due to interfacial adsorption in mother plugs and the largest daughter droplets from the average bulk rate is consistent with previous reports in the literature describing well-passivated aqueous-oil interfaces in microfluidic devices.[11] What, then, is different about the splitting-off process described in this paper for forming daughter droplets in the second T-junction from the more established assays for detecting nonspecific enzyme adsorption? How can we rationalize why the NP-PEG surfactant appears to passivate the oil-water interface adequately only for the larger size droplets and plugs?

First, for interfacial tension measurements using the pendant drop technique, drops were formed by slowly extruding aqueous solution into a quiescent oil phase, so there was little shear stress exerted on a growing drop due to the gradient of the flow field compared to the shear stress experienced by daughter droplets at the second T-junction in our microfluidic device.

Second, it is not possible to quantitatively compare the stresses present during the formation of the microemulsion droplets used in the laser scanning confocal images with the daughter droplets generated on-chip. The emulsions were prepared by rapidly mixing buffer and oil in a micropipette tip, which likely involved turbulent conditions that are difficult to compare meaningfully to simple shear generated in the microfluidic device. However, assuming the same density of β–Gal enzymes in the aqueous interior as at the water-oil interface, based on the homogenous intensity profiles from laser scanning

confocal images of emulsion droplets containing fluorescently labeled enzymes shown below, scaling the S/V ratio corresponding to decreasing daughter droplet diameters in our device results in a higher relative percentage of adsorbed enzymes, based purely on geometrical considerations (see below). This effect is inversely proportional to the cubed root of enzyme concentration in the drops, being ten times greater at nanomolar concentrations than at micromolar concentrations. The concentration of labeled *β*–Gal enzymes in the emulsion was 1.06 μM, while for the droplet experiments in the microfluidic device the enzyme concentration was 1.85 nM. Because of the inherent amplification involved with the use of fluorogenic substrates in enzymatic reactions, monitoring kinetics in droplets was a more sensitive way to detect enzyme adsorption than confocal images of emulsions containing labeled proteins.

Third, intensity profiles from epifluorescent images of Alexa568-*β*-Gal proteins in the daughter droplets generated on-chip were homogeneous, with no evidence for interface adsorption, similar to the laser scanning confocal images of droplets in microemulsions. However, the decreased spatial resolution and increased contributions to the measured intensity in those images from the greater excitation volume compared to laser scanning confocal microscopy lowers the sensitivity for detecting gradients in fluorescent enzyme density across the drop.

Interfacial tension measurements from pendant drops

For interfacial tension measurements, a contact angle goniometer (Ramé-Hart Instruments, Netcong, NJ) with micrometer syringe (Barnant, Barrington, IL) was coupled to a microscope-eyepiece digital camera (EM-500M, Big Catch, Torrance, CA) to capture images of pendant droplets. All glassware and metal blunt-tip needles (Hamilton, Reno, NV) were cleaned in warm (45-50° C) RBS 35 detergent solution (Pierce, Rockford, IL) for two hours and rinsed with Millipore water thoroughly before drying at 80° C overnight in an oven. Because the density of the aqueous solution was greater than that of soybean oil, aqueous pendant droplets were formed in the oil phase. A quartz cuvette (Hellma, Plainview, NY) containing 700 μl soybean oil, purified by passage through a fluorisil column, was

placed on the 3-axis stage of the goniometer. The glass micrometer syringe, containing aqueous solution, with the luer-lock metal needle attached, was carefully lowered into the cuvette until the blunt tip of the needle was immersed a few mm into the oil. After focusing the camera on the tip of the needle, 2 – 4 μl aqueous solution from the syringe was carefully extruded into the oil phase to form a droplet at the needle tip. Images were captured at 10 second intervals starting immediately after the formation of the droplet. These images were processed with ImageJ software and fit with an axisymmetric drop shape analysis program to get a numerical solution for the interfacial tension from the Young-Laplace equation.[12] For each set of conditions (e.g. varying the concentration of NP-PEG surfactant in the oil phase), three to five identical measurements were made in order to obtain reliable statistics. The effective aspect ratio and magnification of the imaging set-up was calibrated by imaging a 0.125 inch steel ball bearing affixed to the end of a blunt metal needle with epoxy and immersed in the oil-filled cuvette. The interfacial tension of aqueous pendant drops in purified oil including NP-PEG surfactant at the concentration used in the microfluidic experiments (0.1% v/v) was 7.5 mN/m. As a check, the surface tension from a droplet of 18 MΩ water in air was determined to be 72.8 mN/m, which agreed with literature values.[13]

Figure S13A and B are plots of the interfacial tension (IFT) from μL aqueous pendant drops suspended in the oil phase, with and without NP-PEG surfactant, respectively. Even in the absence of NP-PEG in the oil phase (Figure S13A), differences in the IFT values due to protein adsorption could not be detected beyond the measurement uncertainty (standard deviation) for droplets containing 1.0 μg/mL β-Gal enzymes compared to droplets containing only reaction buffer. With 0.1% v/v NP-PEG included in the oil, the minimum protein concentration needed to detect a change in measured IFT was 100 μg/mL, two orders of magnitude greater than that used for the on-chip experiments.

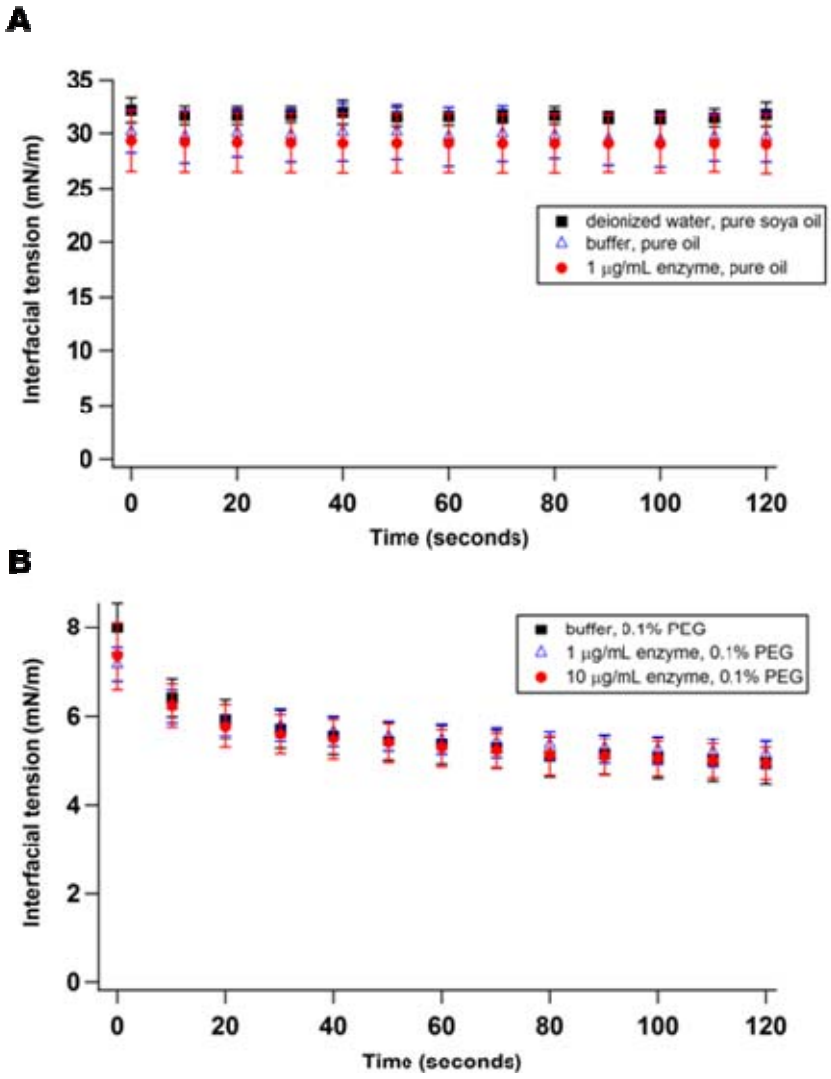

Fig. S13 Interfacial tension (IFT) measurements from pendant aqueous drops suspended in oil phase. IFT data without (A) and with (B) 0.1% v/v NP-PEG surfactant included in the oil.

Laser scanning confocal microscopy images of microemulsions

In order to study nonspecific adsorption of enzymes at the water-oil interface, β−Galactosidase was labeled by Alexa Fluor 568 using the Protein Labeling Kit (Molecular Probes, Carlsbad, CA). Microemulsions were formed by mixing in a micropipette tip aqueous buffer containing labeled proteins with purified soy oil containing 0.1% v/v NP-PEG surfactant. The emulsion was delivered to a # 0 glass cover slip and images were taken on an Axiovert 100 M inverted microscope, configured for confocal laser scanning microscopy (CLSM) (LSM 5 PASCAL, Zeiss), and equipped with a Plan-Neofluar 63X

objective lens (1.25 NA). The pinhole was set to 120 μm (2.0 Airy units), and detector gains were set at 800 V for both red and green channels. The images were recorded as 16-bit tiff files and processed using the Metamorph version 7.0r2 (Universal Imaging Corp, Downington, PA), and ImageJ software.

Figure S14A and B are confocal images of 20 μm diameter droplets in water-in-oil microemulsions containing 570 μg/mL (1.06 μM) fluorescently labeled Alexa568-*β*-Gal enzymes, without (A) and with (B) the presence of 0.1% v/v NP-PEG surfactant in the oil phase. Since the images in Figure S14 are from individual z-slices, we assumed that there were negligible contributions to the measured intensities from voxels that were out of the focal plane. The lack of discernible fluorescent contrast at the periphery of the droplet in Figure S14B when NP-PEG surfactant is present indicates effective passivation of the interface with NP-PEG.

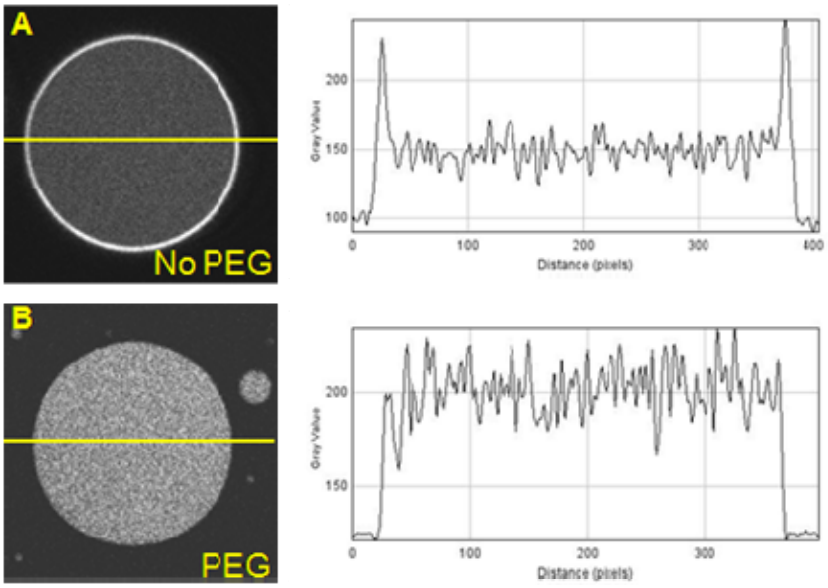

Fig. S14 Laser scanning confocal fluorescent images of water-oil microemulsions containing 1.06 μM Alexa568-*β*-Gal enzymes without (A) and with (B) 0.1% v/v NP-PEG surfactant in the oil phase. Droplet diameters 20 μm.

S/V scaling of enzyme densities in droplets

We used the confocal image of fluorescently labeled β-Gal enzymes in Figure S14B as a starting point for estimating how increasing the S/V ratio in water-in-oil droplets would change the relative percentage of proteins nonspecifically adsorbed at an interface, assuming the density (mol/m^2) of enzymes at the interface and in the interior of the droplet remained equal. This assumption places an upper bound for the number of Alexa568-*β*-Gal enzymes that could be adsorbed at the interface relative to that in the aqueous interior and still result in a uniform line profile of fluorescence intensity observed in Figure S14B. The concentration of Alexa568-*β*-Gal enzymes used was 1.06 μM, which translates to 6.02 x 10^{20} enzymes per m^3. The equivalent territorial volume per enzyme is the inverse of this number, 1.66 x 10^{-21} m^3/enzyme, with radius 73.5 nm. The corresponding territorial area per enzyme at the interface is 1.70 x 10^{-14} m^2/enzyme, which results in a molar surface density (Γ) at the interface of 9.80 x 10^{-11} mol/m^2. The number of enzymes at the interface in moles is this number multiplied by the surface area of the droplet (e.g. 4.19 x 10^{-10} m^2 for the 20 μm diameter droplet used in Figure S14B). Thus, the maximum percentage of enzymes at the interface (4.10 x 10^{-20} moles) relative to the total (4.19 x 10^{-18} moles), was slightly less than 1% for the droplet shown in Figure S14B.

By simple scaling of these numbers with an increasing S/V ratio, the relative percentage of interface-bound enzymes increases. Figure S15A plots this relative percentage as a function of increasing S/V ratio for four different nominal enzyme concentrations (10^{-6} M to 10^{-9} M). The lowest S/V ratio for Figure S15 A and B (10^5 m^2/m^3) corresponds to the 20 μm spherical drops imaged in Figure S14, and roughly to the aqueous mother plugs in the main channel of the microfluidic device (30 μm width and height, with lengths varying from 70 to 90 μm, depending on flow rate). The highest value of the S/V ratio corresponds to 4 μm diameter daughter droplets generated on-chip.

Increasing the S/V ratio by a factor of five results in increasing the relative percentage of interface-bound enzymes by a factor of five as well, for each concentration plotted in Figure S15A. However, a much higher proportion of the total enzyme population would be interface-bound at nanomolar

concentrations than at micromolar concentrations, for all S/V ratios. This is because the ratio of the number of interface molecules to the total number of molecules is equal to $\frac{S \cdot c^{2/3}}{V \cdot c} = \frac{S}{V} \cdot c^{-1/3}$, where S is the surface area of the interface, V is droplet volume and c is concentration. Hence, the relative percentage of interface-bound enzymes increases by a factor of ten in going from micromolar to nanomolar concentrations. At nanomolar concentration, almost half of the total enzyme population for a 4.0 μm diameter droplet would be bound to the interface, when the enzymes in the interior and the interface are at the same density.

The top trace in Figure S15B is an estimate of how the concentration of β-Gal enzymes remaining in the aqueous interior of a daughter droplet, presumed to be the only enzymes that are catalytically active, decreases with increasing S/V ratio, assuming a nominal starting concentration of 1.85 nM (1 μg/mL). For comparison, the bottom trace is the effective concentration of active enzymes that would result in the initial rate data presented in Figure 2B of the paper, estimated by solving for $[E]_0$ from the Michaelis-Menten formula,

$$[E]_0 \approx \left[\frac{K_M + [S]_0}{[S]_0} \right] . \frac{V}{k_{cat}},$$

with K_M = 128.5 μM and k_{cat} = 1341 s^{-1}. V is the initial reaction rate data from Figure 2B, and the approximation $[S](t) \approx [S]_0$ = 25 μM should be valid at early times. Comparison of the two traces indicates that S/V scaling alone does not fully explain the four-fold loss of enzyme activity in daughter droplets compared to the bulk initial rate. It does, however, offer a partial explanation for why the larger droplet in Figure S14B, with a higher concentration of labeled enzymes, was not as sensitive an assay for protein adsorption at the interface than the reaction rate data from the smaller daughter droplets generated by shear in the T-junction of the microfluidic device.

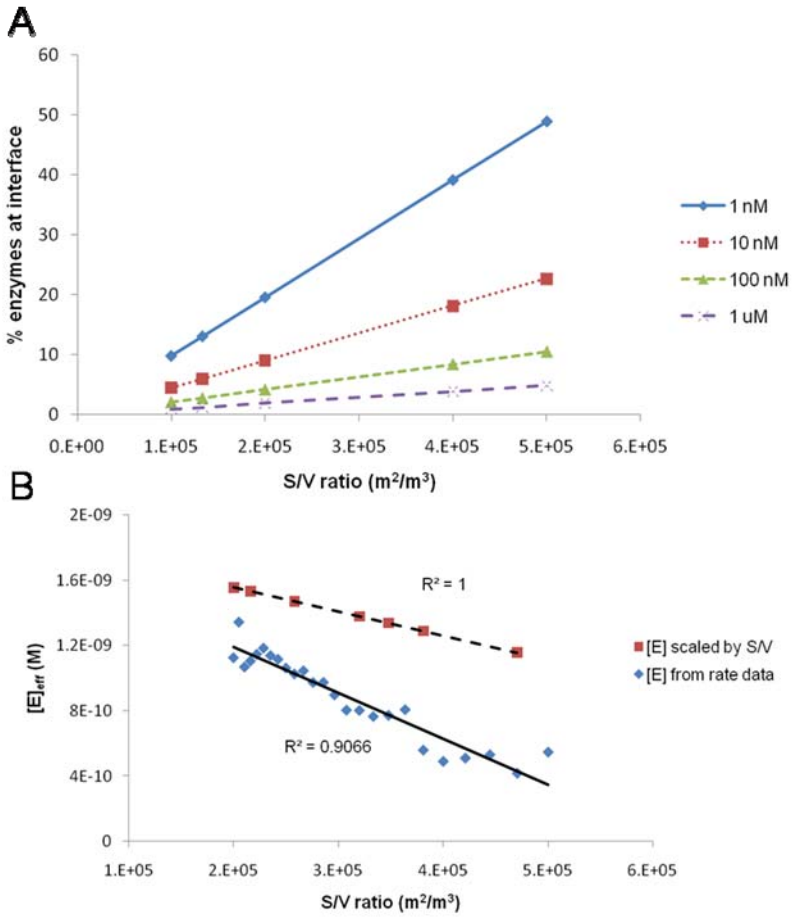

Fig. S15. (A) Relative percentage of total enzyme population adsorbed at the interface, as function of S/V ratio and concentration, assuming the same density of enzymes (mol/m^2) throughout droplet. (B) Effective concentrations of active enzymes left in aqueous interior of droplet after interface adsorption (1.85 nM nominal concentration), using S/V scaling (dashed line), and initial reaction rate data from Figure 5B of the paper (solid line).

Epifluorescent images of daughter droplets containing labeled enzymes

Figure S16 shows that the fluorescence intensity profiles from Alexa568-β-Gal proteins in the daughter droplets were homogeneous, with no evidence for interface adsorption, similar to the laser scanning confocal image in Figure S14B. However, the decreased spatial resolution and increased contributions to the measured intensity in the image from the greater excitation volume with

epifluorescence microscopy compared to laser scanning confocal microscopy lowers the sensitivity for detecting gradients in fluorescent enzyme density across the drop in Figure S16.

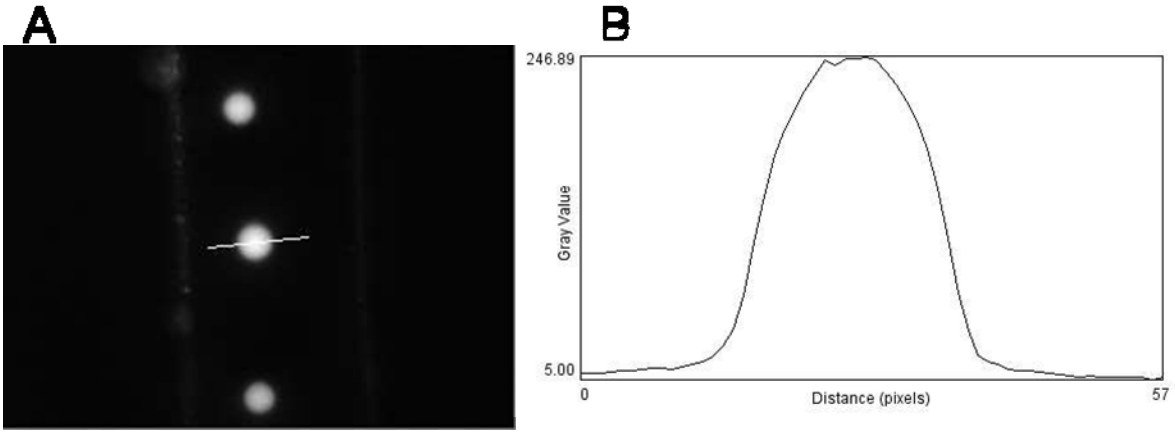

Fig. S16 Epifluorescent microscope image (A) and line scan (B) of 5 μm daughter droplets containing 13 μg/mL Alexa568–*β*–Gal enzymes .in the side channel.

Calculation of p-value using student t-test in Figure 2B of main text

In Figure 2B, the reaction rate was fitted to a linear function of daughter droplet diameters using Matlab and the p-value using t-test was obtained by the built-in Matlab function "regstat".

Raw data for Figure 2B of main text

Raw data is included in the file, "SI Raw Data Figure 2B.pdf" uploaded as Supporting Information.

References

1. Huebner, A.; Srisa-Art, M.; Holt, D.; Abell, C.; Hollfelder, F.; deMello, A. J.; Edel, J. B. *Chem. Comm.* **2007**, 1218-1220.

2. Meng, Y.; High, K.; Antonello, J.; Washabaugh, M.W.; Zhao, Q. *Anal. Biochem.* **2005**, *345*, 227-236.

3. Copeland, R.A. *Enzymes: A Practical Introduction to Structure, Mechanism, and Data Analysis*, Wiley-VCH: New York, 1996.

4. Jung, S.-Y.; Liu, Y.; Collier, C.P. *Langmuir* **2008**, *24*, 4439-4442.

5. Di Noto, V.; Lavina, S.; Longo, D.; Vidali, M. *Electrochim. Acta* **1998**, *43*, 1225-1237.

6. Thorsen, T.; Roberts, R. W.; Arnold, F. H.; Quake, S. R. *Phys. Rev. Lett.* **2001,** *86*, 4163-4166.

7. Zhou, H. X.; Rivas, G.; Minton, A. P. *Annu. Rev. Biophys.* **2008,** *37*, 375-97.

8. Vergara, A.; Paduano, L.; D'Errico, G.; Sartorio, R. *Phys. Chem. Chem. Phys.* **1999***, 1,* 4875-4879.

9. Schnell, S.; Turner, T. E. *Prog. Biophys. Mol. Biol.* **2004**, *85*, 235-260.

10. Minton, A. P. *J. Biol. Chem.* **2001**, *276*, 10577-10580.

11. Roach, L.S.; Song, H.; Ismagilov, R.F. *Anal. Chem.* **2005**, *77*, 785-796.

12. Busoni, L.; Carlà, M.; Lanzi, L. *Rev. Sci. Instr.* **2001**, *72*, 2784-2791.

13. CRC Handbook of Chemistry and Physics, 79th ed.; CRC Press: Boca Raton, 1998.